Version of Record: https://www.sciencedirect.com/science/article/pii/S0169433222028422
Manuscript_6c235228491639a96697aea3eede0956

Modification of Conventional Peak Shapes to Accurately Represent Spectral Asymmetry: High-Resolution X-ray Photoelectron Spectra of $[C_4C_1Pyrr][NTf_2]$ and $[C_8C_1Im][NTf_2]$ Ionic Liquids

Emily Smith,[1] Neal Fairley,[2] Peter Licence,[1,3] Robert Jones[1] and Jonas Baltrusaitis[4,*]

[1]School of Chemistry, The University of Nottingham, Nottingham NG7 2RD, UK

[2]Casa Software Ltd, Bay House, 5 Grosvenor Terrace, Teignmouth, Devon TQ14 8NE, UK

[3]University of Nottingham, GSK Carbon Neutral Laboratory for Sustainable Chemistry, Nottingham NG7 2RD, UK

[4]Department of Chemical and Biomolecular Engineering, Lehigh University, 111 Research Drive, Bethlehem, PA 18015, USA

Abstract

X-ray photoelectron spectroscopy (XPS) is one of the most widely used techniques for surface characterization. Analysis of XPS data is challenging and requires the analyst to fit the data with synthetic line shapes to reach physically meaningful interpretations. Experimental spectral envelopes, however, are complex and display asymmetric features that are often ignored or attributed to additional chemical components. The high-resolution XPS spectra of $[C_4C_1Pyrr][NTf_2]$ and $[C_8C_1Im][NTf_2]$ all exhibit a degree of asymmetry which is systematically observed at the higher binding energy side of photoemission envelopes. We present the development of a refined fitting procedure for XPS spectra of these ionic liquid-based systems which include (a) Shirley background offset necessary to account for the insulator-like region and (b) spectral asymmetry in C 1s and N 1s regions. Further, Shirley and trapezoid components are applied to compensate for inelastic scattering taking place during electron transitions as high as 7.8 eV above the start of the fitting region in C 1s high-resolution spectrum. To demonstrate the fitness of this model, we present an analysis of a 2:1 mixture of $[C_4C_1Pyrr][NTf_2]$: $[C_8C_1Im][NTf_2]$.

*Corresponding author: job314@lehigh.edu; +1-610-758 6836

Keywords: XPS; ionic liquids; peak model; Voigt; asymmetry; Shirley

© 2022 published by Elsevier. This manuscript is made available under the Elsevier user license
https://www.elsevier.com/open-access/userlicense/1.0/

Introduction

Ionic liquids (IL) have gained significant attention due to their unique properties and applicability in numerous chemistry and engineering-related fields including catalysis [1,2], liquid mediation extraction and separations [3] as well as energy storage and harvesting applications [4]. There has also been a significant focus on surface and thin film-related applications such as lubricant additives [5] due to their interesting behavior at cold and working temperatures, degradation and breakdown products, and reactivity necessitating new analysis methods to be developed that can analyze liquid surface composition. In general, attempts to study the liquid phase using X-ray photoelectron spectroscopy (XPS) were limited by the evaporation rate of the liquids and interference from the gas phase [6,7] and advances in surface science focused on analyzing liquids by modifying experimental setup via the introduction of liquid jets [8] or so-called ambient pressure XPS [9]. In the early 2000s researchers recognized that due to their extremely low vapor pressure, ILs could be placed in UHV with no instrument modifications similar to solid samples which allowed routine and repeatable measurements of the liquid phase.

Since 2005, there has been a large body of work published using XPS and other UHV techniques to study ILs [10–12]. For example, angle-resolved XPS (AR-XPS) was used to study the upper surface of the IL in a vacuum of both deposited (bulk) droplets and thin-film monolayers due to the low vapor pressure of the ILs. Changes in the relative intensity of peaks in the spectra for different angles of electron collection can be indicative of enrichments or depletions of the elements in the uppermost layers of the IL-vacuum interface. Lockett *et al.* examined surface ordering and formation of electrical double layers at the liquid vacuum interface of imidazolium ILs performing further studies with synchrotron-based XPS for various 3-methylimidazolium tetrafluoroborate - $[C_nC_1Im][BF_4]$ - ILs and found a similar correlation with longer aliphatic chains being closest to the vacuum interface [13–15]. Pyrrolidinium-based ILs with increasing aliphatic chain lengths, as shown in Figure 1, analyzed via XPS showed the aliphatic groups are preferentially enriched at the IL-vacuum interface on average above the ionic constituents [16]. Maier and coworkers applied AR-XPS to study surface enrichment of the ethylene glycol functionalized imidazolium-based ILs [17] as well as a range of imidazolium ILs with different anion sizes [18] and noted that the aliphatic chains attached to the imidazolium ring tend to preferentially segregate at the vacuum interface for the smaller anion species ILs; however, as the anion size increased segregation diminished and the measured compositions were closer to the bulk values. The same authors also performed several

studies *in-vacuo* using physical vapour deposition (PVD) to obtain thin films of $[C_1C_1Im][NTf_2]$ and $[C_4C_1Im][NTf_2]$ on mica surfaces and $[C_1C_1Im][NTf_2]$ and $[C_8C_1Im][NTf_2]$ on Au(111) on mica [19,20]. These studies utilized AR-XPS measurements and concluded that PVD can be used to deposit complete, undamaged IL ion pairs that adsorb onto the surface initially to form a complete thin film of ~1 monolayer thickness, defined as either a single layer of coplanar positive and negative ions or a double layer of IL with positive and negative ions in two layers. For subsequent deposition, island-like growth was observed rather than a layer-by-layer mechanism. Recently, the same group utilised electrospray ionisation (ESI) to successfully deposit $[C_8C_1Im]Cl$ and $[C_8C_1Im][NTf_2]$ onto Au (111) surfaces [21,22]. The ILs initially exhibited growth best described in a single chequerboard (alternating ion species) arrangement layer followed by island growth for the $[C_8C_1Im]Cl$ and layer-by-layer growth for the $[C_8C_1Im][NTf_2]$. $[C_1C_1Im][NTf_2]$ was deposited onto a Ni (111) substrate using PVD and was shown using AR-XPS to exhibit a slightly different growth mechanism to the Au(111), with the cations initially being closer to the metal-IL interface and the anions on top. After ~ 0.4 ML they start to form a chequerboard alternating arrangement. For the clean Ni (111) the IL can be desorbed by heating, for the oxidized surface desorption of the cation only occurs, leaving the $[NTf_2]^-$ anions *in situ*. This highlights the fact that surface interaction is defined by the uppermost layer of the substrate and will depend strongly on the oxidation of the surface or the presence of adsorbed contaminants [23]. In general, XPS studies of ILs with common anion are rather rare [24] but have been performed to exert the effects of the cation acidity on the electronic environment of the anion.

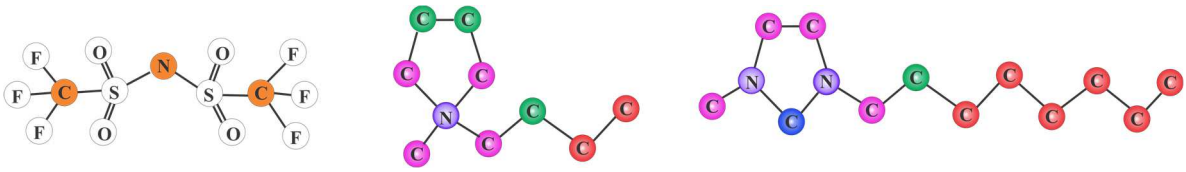
Due to the ionic nature of the IL components, many charge-related phenomena were observed in the presence of X-rays, including charging of their surfaces [25] which resulted in a shift of the measured binding energies in XPS spectra with no changes in the overall IL chemical composition. In principle, ILs are insulators as they have a band gap, but they also are electrically conducting due to ionic mobility and capacitance/electrolysis at electrodes. This is substantiated by the fact that, when frozen to a glass or a crystal, ILs become non-conducting thus showing that they are indeed insulators. Despite conducting nature of the ILs, their background shape in spectra was 'insulator-like', *i.e.* it has a long flat spectral region. Furthermore, an asymmetry exists to the higher binding energy side of IL XPS peaks which has not been routinely included in the IL peak fits. Conducting samples, such as graphene oxide, exhibit asymmetric peaks because of the electron promotion to their conduction bands during emission [26]. Peak asymmetry has been an important consideration for many years [27][28]

and this work presents the developments needed to accurately fit ionic liquid XPS spectra including (a) Shirley background offset necessary to account for the insulator-like region and (b) spectral asymmetry in C1s and N1s regions. In particular, for the experimental data presented in this paper, the asymmetric peak shapes were developed which apply to all element chemically shifted peaks in a spectrum, transferrable across different IL samples. Also, the Shirley background idea has been extended with an energy offset that accommodates the insulator-like behavior of ILs.

Peak models presented in this paper make use of line shapes that include parameters that can be adjusted to alter the shape characteristics of line shapes. These line shapes are used because there is a close relationship between these asymmetric curves and a true Voigt function. The parametric form for these line shapes allows optimization to be performed that fits peak models to data by focusing on specific adjustments to a parameter and then observing in terms of figure-of-merit for a fit and visual assessment for the consequences of a particular line-shape-parameter. Results from these optimization steps designed to provide best-fit line shapes for data also provide information to allow outputs from fitting peak models to data to be assessed such as area or FWHM for component peaks. The results of performing an analysis by optimizing line-shape parameters are presented and commended as a method for constructing peak models which offer best-fit solutions that are also best-fit physical solutions.

Experimental

Materials: IL samples were prepared in the laboratory via established synthetic methods [29]. The purity of all IL samples was independently assessed using ^{1}H NMR and ^{13}C NMR spectroscopy. The structures of the RTILs investigated are detailed in Figure 1. In this work, we used bis[(trifluoromethane)sulfonyl]imide $[NTf_2]^-$ salts of the often studied 1-butyl-1-methyl-pyrrolidinium $[C_4C_1Pyrr]^+$ and 1-octyl-3-methyl-imidazolium $[C_8C_1Im]^+$ cations.



(a) $[NTf_2]^-$ (b) $[C_4C_1Pyrr]^+$ (c) $[C_8C_1Im]^+$

Figure 1: *Molecular structures of bis[(trifluoromethane)sulfonyl]imide* $[NTf_2]^-$*, 1-butyl-1-methyl-pyrrolidinium,* $[C_4C_1Pyrr]^+$*, and 1-octyl-3-methyl-imidazolium,* $[C_8C_1Im]^+$*. C and N atom colors represent peaks used to fit the lineshapes shown in* ***Figure 5*** *and* ***6****, respectively.*

X-ray Photoelectron Spectroscopy: The experimental details for the analysis of the ILs using XPS have been published previously [25,30,31]. Briefly, XPS spectra were recorded using a Kratos Axis Ultra spectrometer equipped with a monochromated Al Kα X-ray source ($h\nu$ = 1486.6 eV), hybrid (magnetic/electrostatic) electron beam path optics, a hemispherical analyzer, a multichannel plate, and a Delay Line Detector (DLD) with a collection angle of 30° and a takeoff angle of 90°. The X-ray gun power was set to either 100 or 150 W, dependent on the quality of the vacuum obtained. All spectra were recorded using an aperture slot of 300 × 700 μm^2 with a pass energy of 80 eV for survey scans and 20 eV for high-resolution core-level scans. All XPS spectra were recorded using the Kratos VISION II software; data files were translated to VAMAS format. During the experiments, no charge compensation was used and the samples were grounded. Calibration of the energy range is performed using Au 4f 7/2, Ag 3d 5/2 and Cu 2p 3/2 peaks. No charge correction in software is performed and spectra are presented using the apparent binding energy for photoemission defined by the apparatus. The samples were mounted as droplets onto the standard stainless steel Kratos sample bar. Each droplet was approximately 3-4 mm in diameter and was prepared with a clean needle dipped into the sample vial. The typical base pressure of the analytical chamber was 3×10^{-9} Torr during scans. All data were processed using the CasaXPS software package (version 2.3.25) [32].

Ionic liquids are an example of samples where instrumental energy resolution is not the limiting factor for the width of photoemission peaks. For these ionic liquid peak models, component FWHM is typically broad compared to the energy resolution of an instrument. Data presented here were measured using pass energy 20 eV in Hybrid lens mode making use of the full slot width on a Kratos Axis Ultra. The FWHM of Ag $3d_{5/2}$ for an Axis Ultra operating in this mode is expected to be close to 0.58 eV. The range of FWHM for components within these peak models for two different ionic liquids is broad (~1.0 eV) by comparison suggesting sample properties rather than instrumental resolution are determining the width and, most likely, the shape of these photoemission peaks.

Theoretical Methods

The Goodness of Fit: For any spectrum, a data vector formed from the intensities of each data channel d_i expressed in vector notation $\boldsymbol{d} = (d_1, \ d_2, \ d_3, \ \ldots \ d_n)$ and the vector of expected values for the data vector $\boldsymbol{e} = (e_1, \ e_2, \ e_3, \ \ldots \ e_n)$, a measure for the deviation of the data vector $\boldsymbol{d}$ from the expected vector $\boldsymbol{e}$ can be written by (1)

$$\chi^2 = \sum_{i=1}^{n} \frac{(d_i - e_i)^2}{e_i} \qquad (1).$$

During optimization, the values of e_i are calculated from a curve that is defined by the summation of a set of component curves representing photoemission and inelastically scattered signal, where each component curve is defined through parameters that are adjusted during the process of optimizing the figure of merit Equation (1). These component curves are defined to model chemical and physical signals only; therefore, the optimum χ^2 for XPS is not equal to zero, but rather a minimum that is consistent with random and systematic variations in spectroscopic data. If data are measured using pulse counting, then for random noise the standard deviation expected for d_i is modeled using Poisson statistics which assumes an uncertainty in each datum is $\sqrt{e_i}$. Therefore, optimization based on minimizing χ^2 for pulse counted data scales data to place equal importance when fitting peak models to data for a high-intensity signal as a low-intensity signal. The consequences for a plot of the residual which is similarly divided by an estimate for $\sqrt{e_i}$ is deviations between the curve after fitting to data and data appear uniform. This uniform appearance for the Poisson scaled residual plot is visual confirmation that minimizing Equation (1) results in a solution curve that fits all data channels equally, which is not necessarily true for a solution the merit of which is solely based on Equation (1).

Optimization based on Equation (1) makes use of the standard deviation expected for pulse-counted data to scale data. Since the magnitude of random noise in pulse-counted data increases as the square root of the counts per bin, random noise in a more intense signal is scaled to a greater extent than in a less intense signal. Hence, in the context of XPS data measured by counting electrons emitted with a given energy, optimization using a figure of merit based on Equation (1) has the advantage that fitting parameters are determined with equal weight for background signal and photoemission signal superimposed on background signal. The goodness of fit used in this work differs from statistics in Equation (1). Rather than reporting the result from optimization, the value for the figure of merit is determined directly from the residual which is normalized concerning noise within each data bin assuming pulse counting for signal. Thus, the standard deviation (SDV) for the resulting residual is reported. Calculating

the figure of merit from the residual as described allows a comparison of different optimization approaches using a common statistic. The label 'chi square' used in this work indicates that the value plotted using the line shape parameter is the normalized residual standard deviation, which for pulse-counted data should approach unity.

Synthetic Line Shapes: A curve that fits data in the least-squares sense defined by Equation (1) can be constructed by a summation of component curves. Each component curve includes parameters that are adjusted during optimization. These parameters are applied through line shapes, which are mathematically defined curves. The selection of synthetic line shapes and the way optimization parameters are introduced through these synthetic line shapes require (for most cases when fitting a curve to data) the use of nonlinear optimization algorithms. In particular, synthetic line shapes may be offset in energy, and the width in energy for a synthetic line shape is scaled by the full width at the half maximum (FWHM) parameter. The act of shifting and scaling the energy distribution defined by a synthetic line shape forces the use of nonlinear optimization. The offset in energy from zero determines the kinetic energy for a component while the scaling in energy is interpreted as the FWHM for a component.

The following definitions make use of mathematically defined shapes using numerical integration that introduces practical limits to these line shapes. Therefore, a distinction is made between mathematical definitions and software-implemented line shapes. For mathematically defined theoretical line shapes Greek characters are used, whereas numerically determined line shapes are distinguished from mathematical concepts by the use of Roman characters.

The term *synthetic* applied to line shapes means a line shape constructed from the following two mathematically defined functions (2) and (3)

$$Lorentzian\colon l(x) = \frac{1}{1+4x^2} \qquad (2),$$

$$Gaussian\colon g(x) = e^{-4ln2x^2} \qquad (3).$$

Voigt-based line shapes can be represented

$$Generalised\ Lorentzian\colon l_g(x\colon \alpha,\beta) = \begin{cases} [(l(x)]^{\alpha} & x \le 0 \\ [l(x)]^{\beta} & x > 0 \end{cases} \qquad (4).$$

$$Lineshape\colon LA(x\colon \alpha,\beta,n) = N\int_{-\infty}^{\infty} l_g(\tau\colon \alpha,\beta)g(x-\tau\colon f_G(n))d\tau \qquad (5),$$

where $f_G(n)$ is the true width for the Gaussian in Equation (5). The parameter n used in Equation (5) to define the line shape is introduced to prevent the interpretation of the line shape as a tool for separating the contributions of the generalized Lorentzian and Gaussian. Correlation between FWHM, synthetic line shape parameters and background curve is the motivation for separating the LA line shape definition from attempting a deconvolution interpretation of the relative widths for the integral operand in Equation (5). Equation (5) provides an asymmetric lineshape where α and β are asymmetry parameters.

Numerically implemented line shapes, for practical reasons, are limited to energy intervals relevant to a given photoemission process. Mathematically, Gaussian and Lorentzian functions are not subject to these practical limitations. Implementing Gaussian and Lorentzian functions involved in numerical integration makes use of upper limits to line-shape parameters which are practically necessary. The value 1401 is one example of a numerical limitation for the upper limit to the width of a Gaussian relative to the width of a Lorentzian used to implement Equation (5). The symmetric line shape $LA(x, m)$ specified by the string LA(m) is constructed from the definition for $LA(x{:}\,\alpha, \beta, n)$ and the maximum allowed value $n = 1401$ defining the width for the Gaussian term in the LA convolution integral in Equation (5)

$$LA(x, m) = LA\left(x{:}\,1{,}1, \left(1401 - \left(\frac{m}{100}\right)1401\right)\right) \qquad (6).$$

Equation (6) is designed to offer a Voigt line shape making use of the parameter m in such a way as to mimic the behavior of pseudo-Voigt line shapes formed from product Gaussian Lorentzian - GL(m) - and sum GL - SGL(m) - combinations of Lorentzian (Equation (2)) and Gaussian (Equation (3)) functions. LA(0) provides a line shape closest to Gaussian, while LA(100) offers a Lorentzian analogously to the commonly used GL(m) and SGL(m) line shapes.

Additionally, the peak models presented in this work make use of components that model background signals. The Shirley algorithm [33] applied to a bell-shaped line shape provides a sigmoid response that can be positioned appropriately to account for the inelastic scattering of electrons for a material with a threshold limit for energy loss. There is clear evidence from materials such as NaCl, SiO_2 and Nylon, for example, that the background signal responds to the position of a photoemission peak only for energies offset from the energy of the zero-energy-loss peak. These materials, as mentioned, also provide examples of spectra where is clear background signal over an extended interval around a photoemission peak is poorly modeled by Shirley approximations. However, in an immediate energy interval centered on a

sigmoid response in the background, before a marked deviation in background signal from a linear response, sigmoid-shaped background approximations positioned offset relative to a linear background offer a plausible explanation for the background signal. A component in a peak model, with energy determined by optimization, allows for the use of line shapes with sigmoid shapes. Similarly, a component that provides a linear background with a gradient determined during optimization models a general trend in background intensity. These components are defined as follows. For any synthetic line shape $F(x)$ a Shirley profile line shape is computed as (7)

$$SB(0)F(x) = \int_x^{\infty} F(\varphi)d\varphi \quad (7).$$

Thus, if $F(x)$ is the Gaussian in Equation (3), and the sigmoid shape formed by the integral in Equation (7) is the shape for the complementary error function. If $F(x)$ is photoemission data after the removal of a Shirley background computed from data, then the result of Equation (7) is the Shirley background computed from data.

A linear component in a peak model is defined using a trapezoid r convoluted with a Lorentzian l of width defined by $h(n)$ where n is an integer.

$$r(x, \alpha, \beta) = \begin{cases} \alpha + (\beta - \alpha)(x + 0.5), & |x| \leq 0.5 \\ 0, & |x| > 0.5 \end{cases} \quad (8),$$

$$TP(x, \alpha, \beta, n) = r(x, \alpha, \beta) * l(x, h(n)) \quad (9).$$

Throughout this work, $n = 0$ in Equation (9) is used which prevents the convolution operation resulting in a component with a linear contribution to a peak model.

Results and Discussion

Intrinsic Asymmetry of Spectral Shapes in ILs: Before looking at particular IL line shapes in detail, it is worth describing the rationale for having line shapes with adjustable parameters. In an ideal experiment, photoemission line shapes originate purely from the physics of the photoemission process. In practice, measured line shapes are influenced by operating modes for XPS instruments. However, for these IL data, pass energy 20 eV hybrid lens mode is not expected to have a significant influence on measured line shapes. More important influences on measured line shape are alterations from the natural line shape caused by the proximity of atoms to other atoms and ions within a material as well as uncertainty in energy for photoelectrons resulting from the ability to measure without bias the energy for electrons. This

is pertinent to data presented in this work which, when measured, has apparent binding energies that differ between measurements as shown in **Figure 2**. Mixtures of $[C_8C_1Im][NTf_2]$ and $[C_4C_1Pyrr][NTf_2]$ were prepared with 10% increase of $[C_4C_1Pyrr][NTf_2]$ and sample 1 pure $[C_8C_1Im][NTf_2]$ and sample 11 pure $[C_4C_1Pyrr][NTf_2]$. All samples were mounted on the same sample bar as droplets and maintained that shape throughout the experiments.

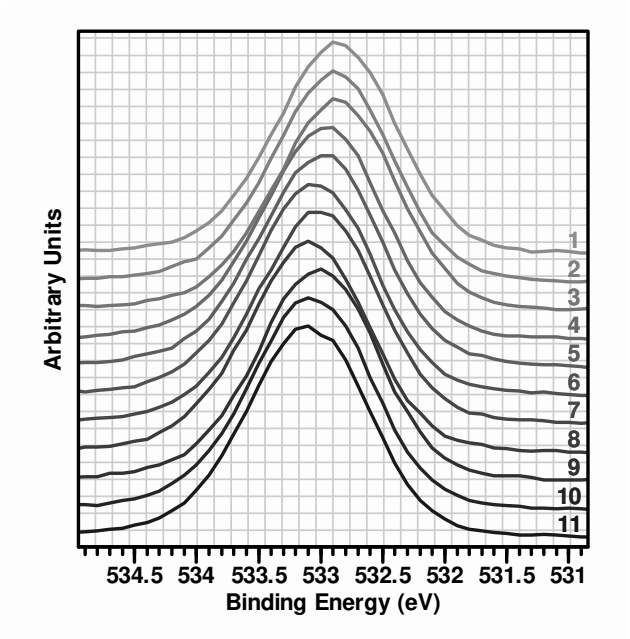


***Figure 2**: O 1s signal displayed using the apparent binding energy obtained when measuring eleven samples of mixed $[C_8C_1Im][NTf_2]$ and $[C_4C_1Pyrr][NTf_2]$. Specifically, sample 1 was 100% $[C_8C_1Im][NTf_2]$, sample 2 was 90% $[C_8C_1Im][NTf_2]$/10% $[C_4C_1Pyrr][NTf_2]$ continuing in 10% increment whereas sample 11 was 100% $[C_4C_1Pyrr][NTf_2]$. Shifts in O 1s peak maxima are consistent with shifts in energy observed for F 1s and S 2p. Hence these energy differences are assumed to be due to differences in the sample potential of each sample.*

Changes in O 1s peak alignment shown in Figure 2 are also present in all narrow scan spectra measured for each sample; therefore, these energy shifts common to all measurements imply each measurement has a distinct potential at the surface that influences the apparent energy for photoelectrons as recorded. Importantly, this suggests that pure symmetric line shapes, routinely used to interpret and quantify IL XPS spectra, are an over-simplified model for photoemission from ILs and provide valid comparative information [34][35], but need to be further rigorously examined. If indeed line shapes with asymmetric character are needed to model photoemission from ILs, then a consideration of to what extent the choice of line shape influences the outcome from a peak model constructed to represent and measure intensities for

chemically-distinct photoemission from ILs needs to be taken. When constructing a peak model, the choice of line shape is important from a mathematical perspective. Fitting a peak model to data using non-linear optimization means minimizing a figure of merit by adjusting parameters defined for each component to the peak model. It is therefore possible to fit a peak model by optimization that includes line shape parameters as part of the optimization steps. However, there are reasons why the application of optimization to line shape parameters is, in general, undesirable. Line shapes are a form of constraint that limits the range of possible solutions available for fitting data. However, line shapes that include parameters relax the constraint applied through the selection of a given line shape. Too much flexibility in line shape parameters allow the fitting of data in a mathematical sense, but the physical meaning associated with the outcome may be damaged by achieving the best mathematical fit. The problem in allowing flexible complex line shapes in which optimization determines the best fit measured solely by some figure-of-merit is analogous to a more familiar problem of fitting spectra with bell-shaped curves. Namely, if no parameter constraints are applied when optimization is performed, a fit may be achieved with components in a peak model that have a non-physical full width at the half maximum (FWHM). In particular, narrow FWHM often occurs since without constraints to FWHM the mathematical best fit accommodates noise rather than being limited to physical shapes. Unfortunately, there is no golden rule for determining if an FWHM is nonphysical. For example, C 1s photoemission from graphite pass energy 20, hybrid lens mode on a Kratos Axis instrument can yield FWHM close to 0.54 eV, while C 1s C=O photoemission measured from Polyethylene terephthalate with these operating modes results in components in a peak model with FWHM greater than 0.85 eV. Similarly, identifying the correct line shape for measured photoemission is difficult to achieve.

Figure 3 shows two examples of line shapes acquired from a 90% $[C_8C_1Im][NTf_2]$/10% $[C_4C_1Pyrr][NTf_2]$ mixture that, when applied to fitting F 1s signal, the response in terms of data reproduction and measured intensity depends on line shape parameters.

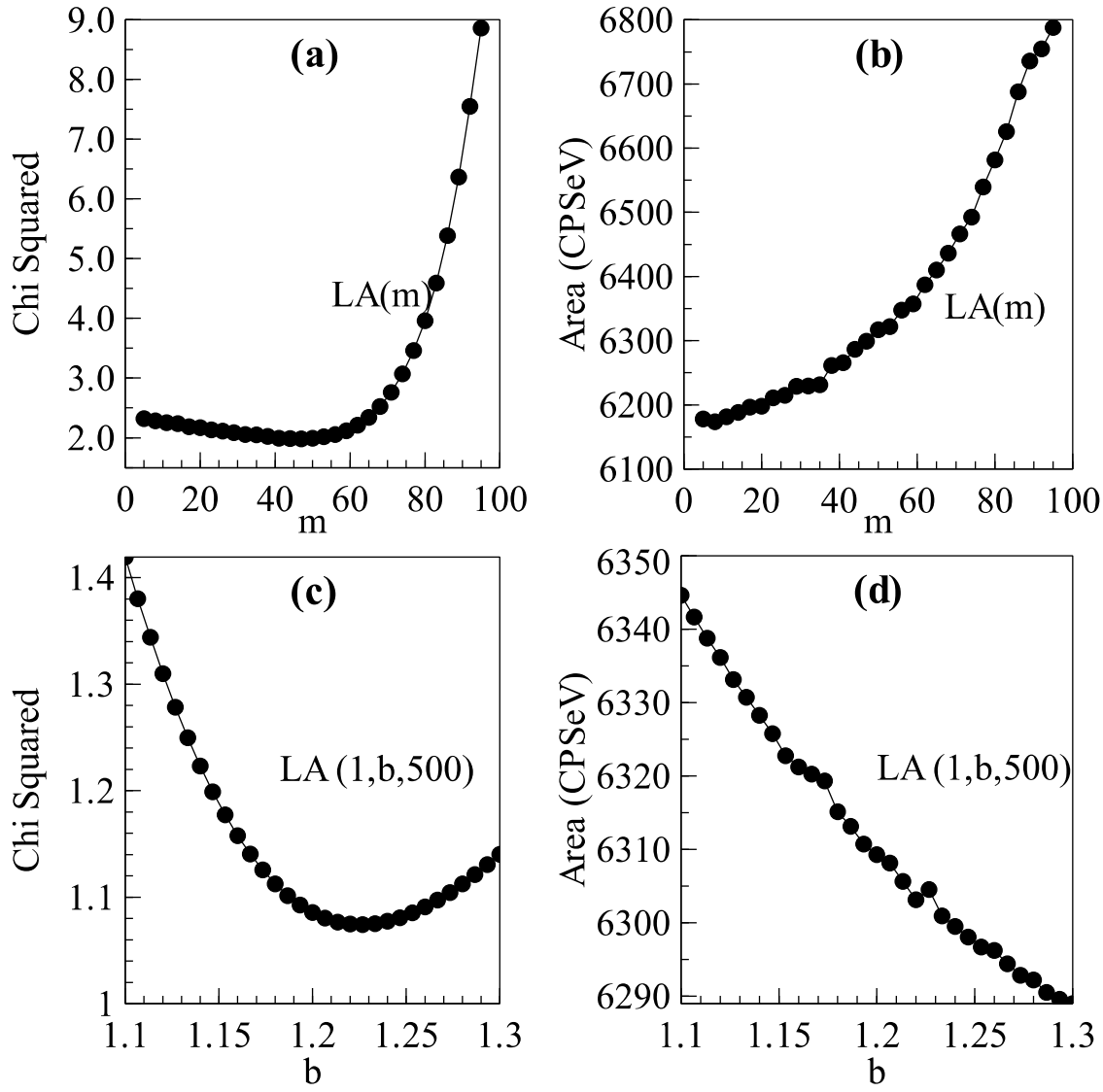


***Figure 3**: A comparison of two line shapes optimized to fit recorded F 1s photoemission line shape from a mixture of 90% [C_8C_1Im][NTf_2]/10% [C_4C_1Pyrr][NTf_2]. (a,b) LA(m) line shape is a symmetric bell-shaped curve numerically calculated using the Voigt function shown in Equation (7). (c,d) LA(1, b, 500) line shape is an asymmetric generalized Voigt function calculated numerically using Equation (5).*

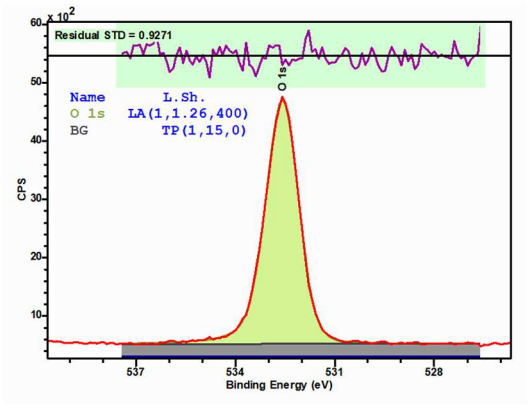
Changes to the symmetrical bell-shaped line shape LA(m) are made by adjusting the parameter m by scanning from pure Gaussian to pure Lorentzian shape. The parameter *m* alters the relative width for the Lorentzian and Gaussian curves that underlie the Voigt function as shown in Equation (6). Adjusting the b parameter (in the LA line shape) over the range of values b in the specific line shape LA(1, b, 500) does not alter the relative widths for the Gaussian and the generalized Lorentzian but rather alters the relative extent of the wings to the left and right of the generalized Lorentzian peak maximum used to calculate the LA(1, b, 500) line shape, as

shown in Equation (5). The range of values for b allows asymmetry to be introduced to a near Voigt-like line shape. The first parameter in LA(1, b, 500) is unity and therefore the left-hand side of the generalized Lorentzian (Equation (4)) is Lorentzian while varying b between 1.1 and 1.3 suppresses the right-hand Lorentzian shape. A convolution of the generalized Lorentzian with a Gaussian of width defined by n = 500 further alters the line shape LA(1, b, 500) resulting in the minimum figure-of-merit, obtained by scanning b, illustrated in Figure 3b. The scan of m in LA(m) is equivalent to performing a scan for n in LA(1,1,n). In this sense, Figure 3a demonstrates how a value for n in LA(a,b,n) can be chosen. For both line shapes displayed in **Figure 3,** the computed area for F 1s alters in response to these two parameters. The point to observe is that the area measured by a component (when fitting to data) depends on the choice of the line shape. Also, note that the figure of merit for the goodness of fit in both cases achieves a minimum, but in the case of LA(m) the minimum indicates data reproduction is limited by the rigid symmetrical line shape definition compared to asymmetry available to LA(1, b, 500) line shape.

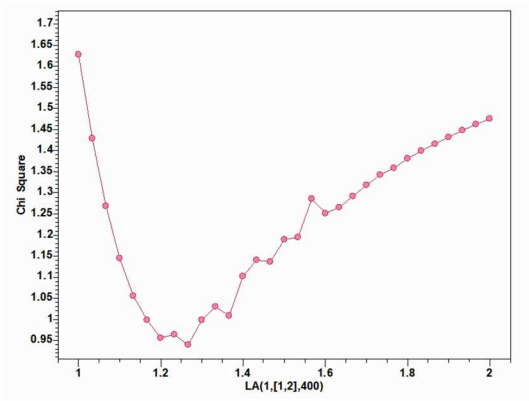
Line shapes that match closely the true measured shape for photoemission signal are highly desirable as these provide the strongest form of guidance to optimization that permits precision in values determined by fitting curves to data. An ability to construct well-formed line shapes requires a degree of flexibility when constructing line shape. However, problems induced by excessive flexibility in line shapes result when non-linear optimization is used to obtain a mathematical fit without sufficient regard for physical properties. Non-linear optimization performs a search through a set of possible solutions available to a peak model defined in terms of parameters. The adjective search is used advisedly since non-linear optimization is performed without the knowledge of what the true optimum might be and a solution is achieved by following a path in an *n*-dimensional parameter space guided by informed choices but guesses. A solution is created by accepting a final set of parameters that are measured in terms of success by a statistic calculated from the model and data. When considered in these terms, optimization even when success is achieved, is achieved with a degree of uncertainty in outcomes. Uncertainty in outputs such as intensity may be exacerbated by permitting parameters for line shapes to be determined through non-linear optimization. For these reasons a strategy for making use of optimization to assist in developing line shapes is required that aids the selection of line-shape parameters but allows informed choices to be made for these parameters rather than total reliance on a statistic to guide a solution. The approach illustrated in **Figure 3** is such a solution. Line shape parameters are determined by supplementing fitting statistics with visualizing the peak model for each line shape parameter after fitting the peak

model to data. Changes to solutions in terms of component binding energy or intensity can be assessed *en route* to determining a solution that conforms to both adequate data reproduction and physically meaningful outputs.

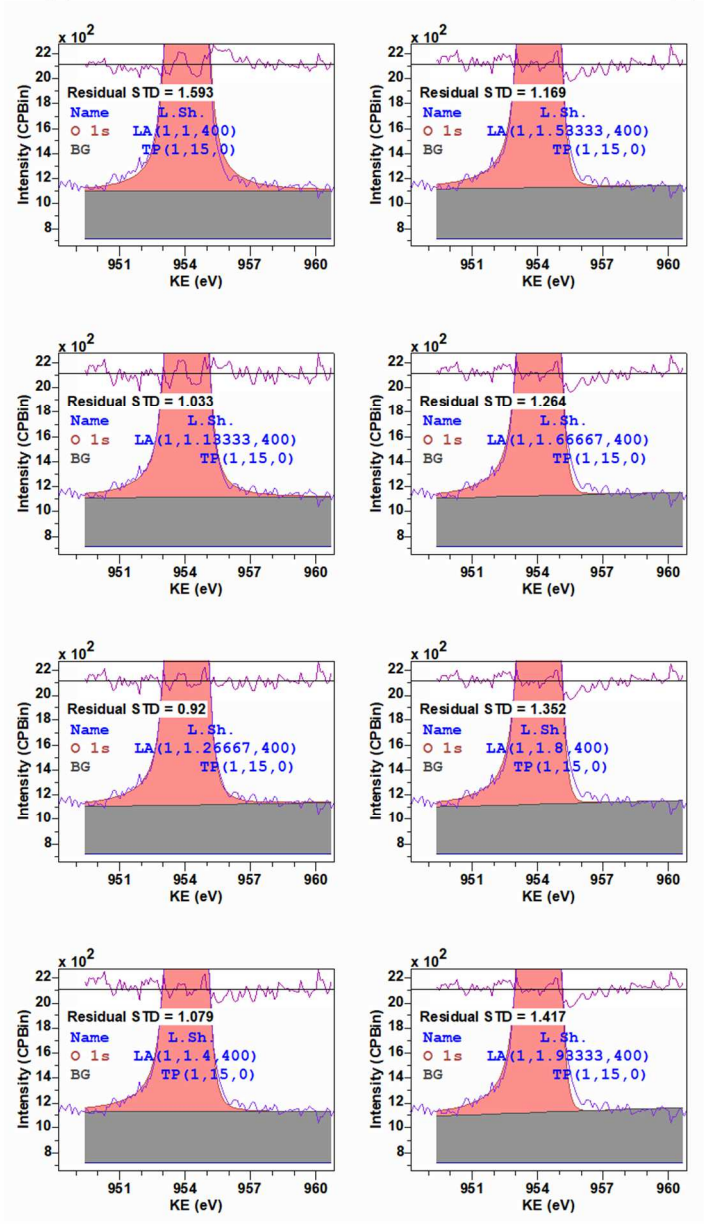
Further analysis of the asymmetry in ILs and application to O 1s, N 1s and C 1s high-resolution spectra. Two ionic liquids, $[C_4C_1Pyrr][NTf_2]$ and $[C_8C_1Im][NTf_2]$, with the molecular structure shown in **Figure 1** and their mixtures were further subjected to spectral analysis. Herein we investigate the model peak shapes for pure ionic liquid samples and apply these to a mixture sample which appears to show that the mixing does not significantly change/perturb the environment that the atoms are in, and thus that the model shapes can be summed/added together to create a total 'mixed spectrum'. While the mechanism of conduction in ILs is not yet fully understood, several mechanisms for conduction have previously been proposed [36] without a definitive conclusion. In XPS, the position of photoelectron peaks from ionic liquids varies with time depending on the IL conductivity, temperature, density and viscosity, typically 0.05 eV per hour, suggesting a build-up of positive charge over time within the surface region of the sample [25]. Therefore, while charge neutralization is not required to perform XPS acquisition for ionic liquids, a charge correction to a reference peak within the ionic liquid is, nevertheless, needed to align the spectra. An intrinsic asymmetry in O 1s high-resolution spectra of ILs is apparent in **Figure 4a** where standard LA shape with α and β parameters set to 1 and Gaussian width is 400 yields residual STD of 1.59 showing poor fit as shown in **Figure 4c**. A systematic introduction of asymmetry by varying β parameter only indeed was observed to result in poor fits as shown in **Figure 4b** and **Figure 4c.** In particular, the symmetric LA (1,1,400) synthetic component resulted in a poor fit on the increasing kinetic energy side while LA(1,1.93333,400) under-compensated on the same side of the peak. The systematic adjustment of β parameters resulted in the minimum chi-squared value of 0.92 with b=1.26667 mathematically and visually showing the right asymmetric shape for this particular O1s peak **Figure 4c**.



(a)



(b)

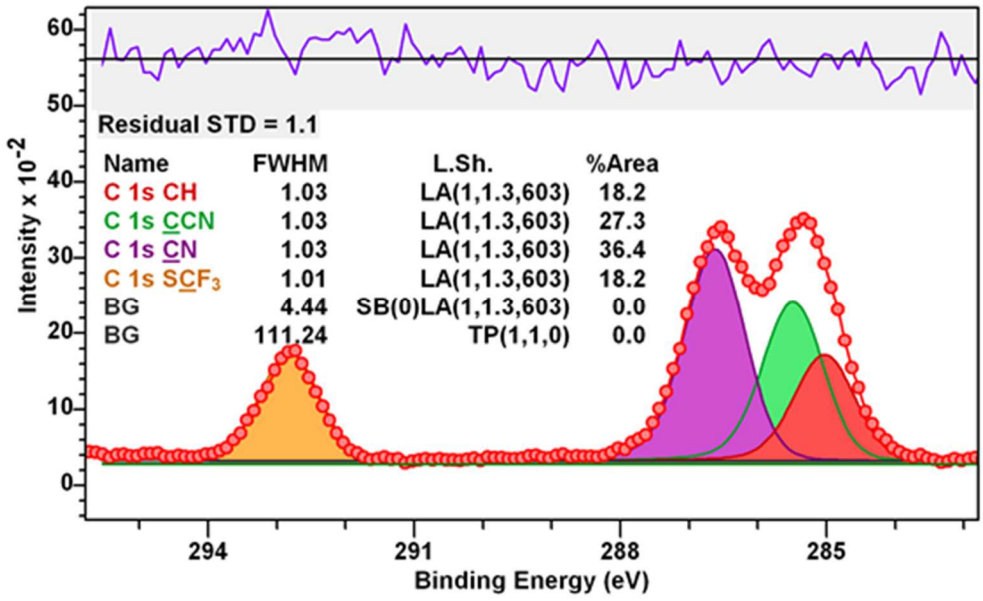


(c)

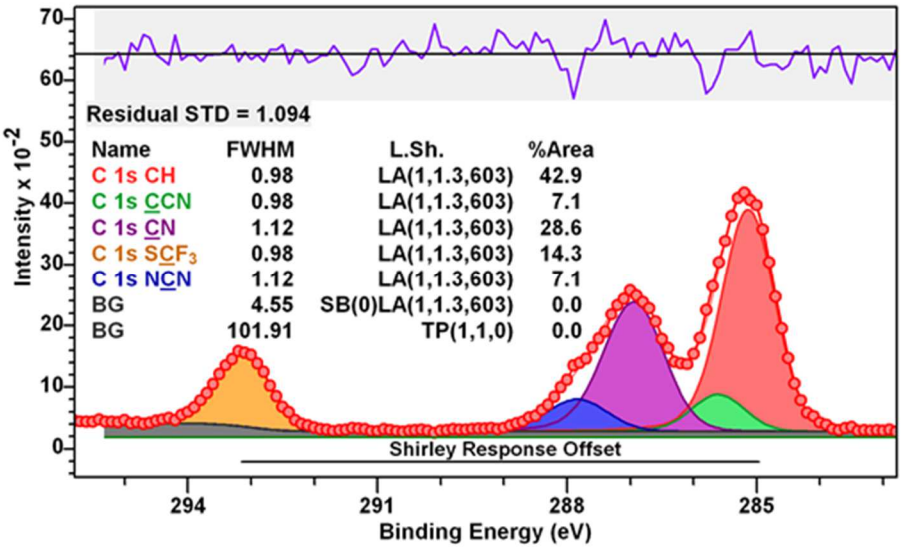
***Figure 4**: (a) Line shape determined for O 1s from 90% [C_8C_1Im][NTf_2]/10% [C_4C_1Pyrr][NTf_2] sample used in **Figure 3**. (b) Figure-of-merit plot in which one line shape parameter is scanned over a range of values. The range of values and the specific parameter*

scanned within the LA line shape is indicated by a pair of values within square brackets [1,2] embedded with the LA line shape definition LA(1,[1,2],400). (c) Examples of asymmetric line shapes sampled from the sequence of fits to data corresponding to the figure of merit plot in (b).

Interestingly, despite 'conducting' ionic liquids background shape in spectra is indeed that of an insulator, in that it has a long flat region, where very little photoelectron interaction occurs within the bandgap, and then the background rises to higher BE away from the photoelectron peak. This background behavior can be seen in **Figure 5** for the C 1s spectra. Both spectra are analyzed into bell-shaped components to the peak model that is constrained in the area to achieve the quality of fit seen in Figure 5 and conform to the expectation for relative proportions of chemical state for carbon within the IL. The measured photoelectron peak shape observed is relatively broad for all elements (F 1s, N 1s, O 1s, C 1s and S 2p) (FWHM ~1.0 to 1.6 eV) and there is a slight asymmetry to high BE for all peaks requiring modification of the commonly used Gaussian/Lorentzian product Gaussian/Lorentzian sum symmetrical peak shapes.



(a)

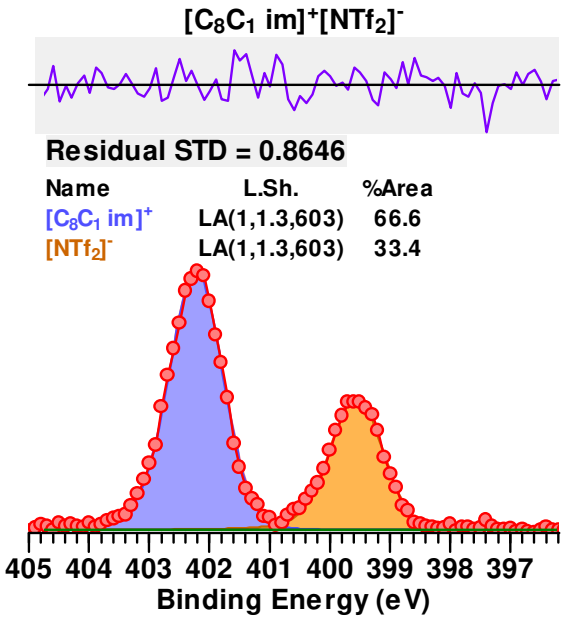


(b)

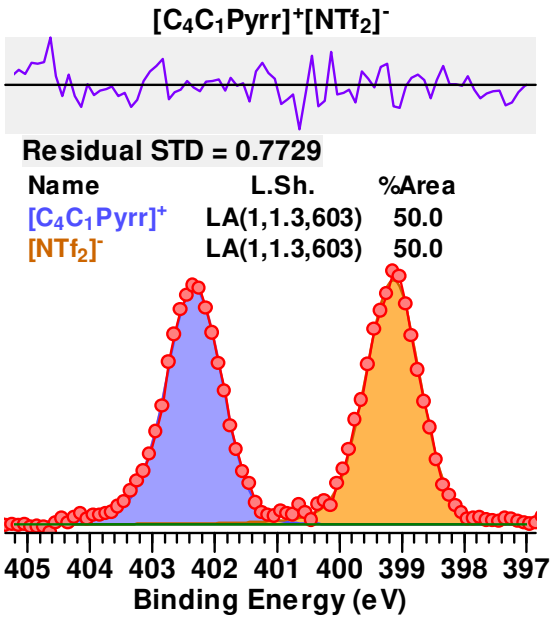
Figure 5: *(a) C 1s peak fitting model constructed for data measured from a sample of pure [C_4C_1Pyrr][NTf_2]. (b) C 1s peak fitting model constructed for data measured from a sample of pure [C_8C_1Im][NTf_2]. These data demonstrate how photoemission from C1s results in a flat background with the first evidence of an increase in background occurring at 7.8 eV offset from CH photoemission appearing underneath C 1s CF_3. This initial rise in the background is assumed to be the result of the inelastic scattering of photoemission with binding energy close to 285 eV.*

The peak model in **Figure 5** makes use of two components that model the background signal. Trapezoid (TP) serves to allow the intensity for a flat background to be determined during optimization. The motivation for introducing TP into the peak model is that without the use of TP the relationship between a background computed from data and data at either extreme of an integration region is determined (as a rule) by averaging data bins at these limits. A user-defined choice for the interval over which a background is defined introduces user bias that can be replaced by fitting TP as part of optimization. The second component is a Shirley sigmoid-shaped component, which like a Shirley background is to some extent dependent on the integration region over which the background is defined. Combining the Shirley and TP components in a peak model limits the influence of the interval selected on optimization outcomes when experimenting with different line shape parameters. Specifically, the background underneath [C_8C_1m] C 1s that is initially flat with a Shirley step offset in energy that occurs beneath [NTf_2] C 1s CF_3 signal (**Figure 5**) is accommodated by a Shirley response calculated from a bell-shaped curve. The height, position and FWHM for the Shirley component in **Figure 5** are fitted as part of optimization. The component representing the Shirley step is

defined by SB(0)LA(1,1.3,603). One further component is included in these peak models in **Figure 5**, namely the offset for a horizontal linear contribution to the background is specified by TP(1,1,0). The offset in intensity defined by TP(1,1,0) is also optimized as part of fitting the peak model to data.Since shapes for components in these peak models for $[C_4C_1Pyrr][NTf_2]$ and $[C_8C_1\ Im][NTf_2]$ shown in **Figure 5** include asymmetry via the line shape LA(1,1.3,603),t would be difficult to justify a specific line shape based on the data envelopes for C 1s for either ionic liquid. However, the same line shape applied to N 1s spectra for these two ionic liquids yields excellent data reproduction indicated by both the residual STD and uniformity of the residual plots shown in **Figure 6**. In case of simple charging effects, which affect the N1s and C1s lines most likely the same way (e.g. adding asymmetry), it is not surprising at all that the same asymmetry parameter 1.3 can be used for successful peak fitting. The point to note about N 1s spectra shown in **Figure 6** is these N 1s component curves are modeled using the same line shape as is used for C 1s in **Figure 5**. In the case of data shown in **Figure 6,** both N 1s peak models reflect the expected relationships for $[C_4C_1Pyrr][NTf_2]$ and $[C_8C_1Im][NTf_2]$. Further, these N 1s components are sufficiently well resolved to assert the line shape LA(1,1.3,603) is a good estimate for the true line shape created for N 1s photoemission from these two ionic liquids. While there is always a degree of uncertainty in the choice of the line shape, the evidence presented suggests asymmetry in a line shape for these samples is important and the generalized Voigt line shape allow suitable peak models for estimating the composition of mixtures formed from $[C_4C_1Pyrr][NTf_2]$ and $[C_8C_1Im][NTf_2]$.



(a)



(b)

Figure 6: *N 1s spectra fit using two components with generalized Voigt line shapes LA(1,1.3,603) for (a) [C_8C_1Im][NTf_2] and (b) [C_4C_1Pyrr][NTf_2]. These peak models and data also demonstrate little or no response in background intensity beneath these photoemission peaks. Background behavior of this nature is typically characteristic of insulating materials and hence linear background was used.*

While the term peak model implies a collection of bell-shaped curves, any peak model necessarily includes curves that are not bell-shaped which are designed to model inelastically scattered background intensity. In many examples involving peak models, background curves are inactive during optimization and are determined from data utilizing specific algorithms such as Shirley [33] or Tougaard Universal [37] backgrounds. An alternative approach to modeling background signals is to include components in a peak model that are active during optimization. The following describes the motivation for and the role played by two such components used to model ionic liquid data in this paper.

The source for the inelastically scattered signal is the photoemission signal that interacts with electrons in ions along the path through the ionic liquid *en route* to the vacuum chamber. These interactions between photoelectrons and bound state electrons in ions require the excitation of bound state electrons in ions. Hence the existence of a bandgap for bound state electrons implies threshold energy below which scattering of photoelectrons fails to excite bound state electrons. It is, for this reason, a background signal with energies close to the energy for a photoemission line from a material with a bandgap does not alter the shape of the background signal until energy is offset from a specific photoemission peak is measured. The response of the background signal to a photoemission peak is often modeled using the Shirley algorithm. A Shirley background approximation provides a sigmoid shape which was designed to model photoemission from a material without a bandgap. Direct use of the Shirley response to a photoemission peak is therefore inappropriate for material with a bandgap. However, the Shirley heuristic may be applied to materials with a bandgap responding to a photoemission peak that is offset in energy from the photoemission peak energy that is generating inelastically scattered electrons. Background signals for ionic liquids are observed to follow the behavior of a material with a bandgap, namely, the background signal is unresponsive to photoemission peaks until threshold energy is passed, at which point the background response may be modeled as sigmoid shape computed from photoelectron data. For these reasons the spectral background associated with photoemission peaks is calculated using a Shirley algorithm where the Shirley

background shape is offset to lower kinetic energy than the kinetic energy for photoemission peaks.

Background signal beneath a photoemission peak is predominantly influenced by inelastic scattering of electrons with kinetic energy greater than the peak of interest. The primary source of background signal is photoemission peaks with kinetic energies greater than the peak of interest. Secondary scattering yields further energy loss for electrons recorded as background signals. For electrons with energies close to the initial photoemission energy, these multiple energy loss events introduce a general shape that influences the background beneath all photoemission peaks with lower kinetic energy. In the case of ionic liquids, the background signal generally increases in intensity as kinetic energy increases. These types of trends in background signal can be locally modeled as a linear background component in a peak model. The gradient for a linear background component in a peak model depends on the proximity of photoemission peaks in a spectrum. On occasion, a constant background beneath photoemission peaks is sufficient to model the background signal. The peak models in **Figure 6** are noteworthy for demonstrating the background response over the energy interval corresponding to these two N 1s photoemission peaks is essentially flat. By contrast, peak models for C 1s signal in Figure 5 include both an active component representing a flat background beneath photoemission peaks and also a Shirley component which is offset in energy from the lowest binding energy C 1s component to model the delayed rise in background signal due to a threshold limit below which inelastic scattering is unlikely.

Peak models shown in **Figure 5** are constructed by making use of area constraints to force the expected stoichiometry for $[C_4C_1Pyrr][NTf_2]$ and $[C_8C_1Im][NTf_2]$. Such an approach is justified because these peak models are not used to understand the materials in question, but rather to create relationships between components that can be used subsequently to analyze related samples. The objective for these peak models was to obtain good data reproduction for data seen in **Figure 7**. The measure for good data reproduction is indicated by the residual STD and visually confirmed using the uniform residual plots in **Figure 7.** It would be unscientific to assume these peak models for C 1s without supporting information from other data as seen in **Figure 5**. The simple peak models in **Figure 6** for N 1s suggest these three forms of ions appear in proportions consistent with the peak models for C 1s. Similar supporting evidence is available from S 2p (not shown here), F 1s and O 1s for these ionic liquids.

In **Figure 7,** the signal associated with different ionic liquids is separated through fitting components to data. Samples prepared with differing proportions of $[C_4C_1Pyrr][NTf_2]$ and

$[C_8C_1Im][NTf_2]$ were created to investigate the response of XPS to mixing ionic liquids with a common $[NTf_2]^-$ ion. Spectra from these samples, of which **Figure 7** represents one example, were analyzed making use of peak models to separate the contributions of these pure forms of ionic liquid to the samples as prepared. However, an analysis using fitting components to data shown in **Figure 7** requires the use of constraints to maintain relationships between components associated with individual ionic liquids. Constraints are needed because these two ionic liquids include photoemission from carbon in similar bond states. Components to a peak model from near-identical binding energy and near-identical FWHM and line shape prevent accurate determination of component area by optimization. Only by enforcing area, FWHM and binding energy constraints within each peak model in **Figure 5** for these two ionic liquids, it is possible to obtain repeatable separation of the signal as shown in **Figure 7**.

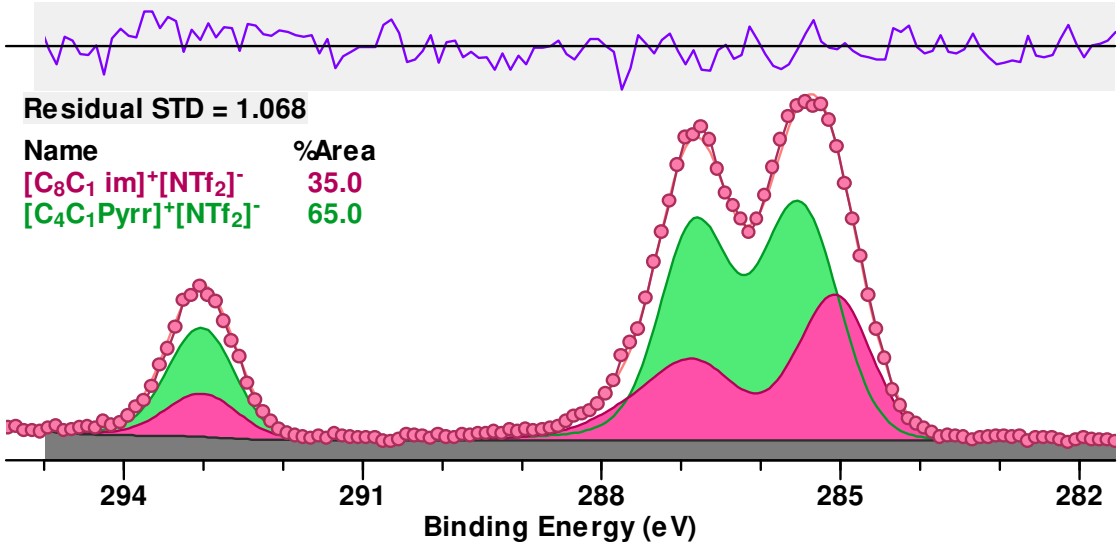


Figure 7: *Peak models designed for data in Figure 5 are combined to form two ensembles describing photoemission signals attributed to two distinct ionic liquids mixed in the proportions* $[C_4C_1Pyrr][NTf_2]$ *:* $[C_8C_1Im][NTf_2]$ *of 2:1.*

Conclusions

The nature and the effect of the peculiar properties of selected ILs under X-rays during the acquisition of XPS spectra are discussed. In particular, the asymmetry in observed peak shapes in $[C_4C_1Pyrr][NTf_2]$ and $[C_8C_1Im][NTf_2]$ spectra was analyzed and presented in this work. This asymmetry was apparent in all the regions measured including F1s, O1s, N1s and C1s. Similarly, energy shifts common to specific measurements suggest spectral shapes and apparent binding energy for raw spectra are determined by the measurement process rather than the

chemical properties of these ILs samples. Under these assumptions, peak models were developed for ILs that account for measurement artifacts using line shapes with parameters optimized under the guidance of sample knowledge. Specifically, the influence of line shapes on physical outputs from fitting peak models to data is demonstrated for F 1s and O 1s photoemission. These results highlight that the choice of line shape alters the measured area when fitted to data. Hence, the choice of line shape is therefore not a mathematical result but should be limited by physical requirements for individual samples.

Acknowledgments

This work was supported as part of the Center for Understanding and Control of Acid Gas-Induced Evolution of Materials for Energy (UNCAGE-ME), an Energy Frontier Research Center funded by the U.S. Department of Energy, Office of Science, Basic Energy Sciences under Award No. DE-SC0012577. PL acknowledges support from the EPSRC (EP/K005138/1, EP/I018093/1, EP/D073014/1 and EP/P013341/1).

References

[1] J.P. Hallett, T. Welton, Room-Temperature Ionic Liquids: Solvents for Synthesis and Catalysis. 2, Chem Rev. 111 (2011) 3508–3576. https://doi.org/10.1021/cr1003248.

[2] T. Welton, Room-Temperature Ionic Liquids. Solvents for Synthesis and Catalysis, Chem Rev. 99 (1999) 2071–2084. https://doi.org/10.1021/cr980032t.

[3] J.G. Huddleston, H.D. Willauer, R.P. Swatloski, A.E. Visser, R.D. Rogers, Room temperature ionic liquids as novel media for 'clean' liquid–liquid extraction, Chem. Commun. (1998) 1765–1766. https://doi.org/10.1039/A803999B.

[4] M. Watanabe, M.L. Thomas, S. Zhang, K. Ueno, T. Yasuda, K. Dokko, Application of Ionic Liquids to Energy Storage and Conversion Materials and Devices, Chem Rev. 117 (2017) 7190–7239. https://doi.org/10.1021/acs.chemrev.6b00504.

[5] Y. Zhou, J. Qu, Ionic Liquids as Lubricant Additives: A Review, ACS Appl Mater Interfaces. 9 (2017) 3209–3222. https://doi.org/10.1021/acsami.6b12489.

[6] H. Siegbahn, S. Svensson, M. Lundholm, A new method for ESCA studies of liquid-phase samples, J Electron Spectros Relat Phenomena. 24 (1981) 205–213. https://doi.org/10.1016/0368-2048(81)80007-2.

[7] H. Siegbahn, K. Siegbahn, ESCA applied to liquids, J Electron Spectros Relat Phenomena. 2 (1973) 319–325. https://doi.org/10.1016/0368-2048(73)80023-4.

[8] B. Winter, M. Faubel, Photoemission from liquid aqueous solutions, Chem Rev. 106 (2006). https://doi.org/10.1021/cr040381p.

[9] M. Salmeron, From Surfaces to Interfaces: Ambient Pressure XPS and Beyond, Top Catal. 61 (2018) 2044–2051. https://doi.org/10.1007/s11244-018-1069-0.

[10] H.-P. Steinrück, Recent developments in the study of ionic liquid interfaces using X-ray photoelectron spectroscopy and potential future directions, Physical Chemistry Chemical Physics. 14 (2012) 5010. https://doi.org/10.1039/c2cp24087d.

[11] H.-P. Steinrück, Surface science goes liquid !, Surf Sci. 604 (2010) 481–484. https://doi.org/10.1016/j.susc.2009.12.033.

[12] K.R.J. Lovelock, I.J. Villar-Garcia, F. Maier, H.-P. Steinrück, P. Licence, Photoelectron Spectroscopy of Ionic Liquid-Based Interfaces, Chem Rev. 110 (2010) 5158–5190. https://doi.org/10.1021/cr100114t.

[13] V. Lockett, R. Sedev, C. Bassell, J. Ralston, Angle-resolved X-ray photoelectron spectroscopy of the surface of imidazolium ionic liquids, Physical Chemistry Chemical Physics. 10 (2008) 1330. https://doi.org/10.1039/b713584j.

[14] V. Lockett, R. Sedev, S. Harmer, J. Ralston, M. Horne, T. Rodopoulos, Orientation and mutual location of ions at the surface of ionic liquids, Physical Chemistry Chemical Physics. 12 (2010) 13816. https://doi.org/10.1039/c0cp00683a.

[15] C. Ridings, V. Lockett, G. Andersson, Effect of the aliphatic chain length on electrical double layer formation at the liquid/vacuum interface in the [Cnmim][BF4] ionic liquid series, Physical Chemistry Chemical Physics. 13 (2011) 17177. https://doi.org/10.1039/c1cp20910h.

[16] S. Men, B.B. Hurisso, K.R.J. Lovelock, P. Licence, Does the influence of substituents impact upon the surface composition of pyrrolidinium-based ionic liquids? An angle resolved XPS study, Physical Chemistry Chemical Physics. 14 (2012) 5229. https://doi.org/10.1039/c2cp40262a.

[17] C. Kolbeck, M. Killian, F. Maier, N. Paape, P. Wasserscheid, H.-P. Steinrück, Surface Characterization of Functionalized Imidazolium-Based Ionic Liquids, Langmuir. 24 (2008) 9500–9507. https://doi.org/10.1021/la801261h.

[18] F. Maier, T. Cremer, C. Kolbeck, K.R.J. Lovelock, N. Paape, P.S. Schulz, P. Wasserscheid, H.-P. Steinrück, Insights into the surface composition and enrichment effects of ionic liquids and ionic liquid mixtures, Physical Chemistry Chemical Physics. 12 (2010) 1905. https://doi.org/10.1039/b920804f.

[19] A. Deyko, T. Cremer, F. Rietzler, S. Perkin, L. Crowhurst, T. Welton, H.-P. Steinrück, F. Maier, Interfacial Behavior of Thin Ionic Liquid Films on Mica, The Journal of Physical Chemistry C. 117 (2013) 5101–5111. https://doi.org/10.1021/jp3115397.

[20] T. Cremer, M. Stark, A. Deyko, H.-P. Steinrück, F. Maier, Liquid/Solid Interface of Ultrathin Ionic Liquid Films: [C 1 C 1 Im][Tf 2 N] and [C 8 C 1 Im][Tf 2 N] on Au(111), Langmuir. 27 (2011) 3662–3671. https://doi.org/10.1021/la105007c.

[21] B. Uhl, T. Cremer, M. Roos, F. Maier, H.-P. Steinrück, R.J. Behm, At the ionic liquid|metal interface: structure formation and temperature dependent behavior of an ionic liquid adlayer on Au(111), Physical Chemistry Chemical Physics. 15 (2013) 17295. https://doi.org/10.1039/c3cp52184b.

[22] F. Rietzler, M. Piermaier, A. Deyko, H.-P. Steinrück, F. Maier, Electrospray Ionization Deposition of Ultrathin Ionic Liquid Films: [C 8 C 1 Im]Cl and [C 8 C 1 Im][Tf 2 N] on Au(111), Langmuir. 30 (2014) 1063–1071. https://doi.org/10.1021/la404429q.

[23] T. Cremer, L. Wibmer, S.K. Calderón, A. Deyko, F. Maier, H.-P. Steinrück, Interfaces of ionic liquids and transition metal surfaces—adsorption, growth, and thermal reactions of ultrathin [C1C1Im][Tf2N] films on metallic and oxidised Ni(111) surfaces, Physical Chemistry Chemical Physics. 14 (2012) 5153. https://doi.org/10.1039/c2cp40278e.

[24] S. Men, P. Licence, Tuning the electronic environment of the anion by using binary ionic liquid mixtures, Chem Phys Lett. 681 (2017). https://doi.org/10.1016/j.cplett.2017.05.049.

[25] I.J. Villar-Garcia, E.F. Smith, A.W. Taylor, F. Qiu, K.R.J. Lovelock, R.G. Jones, P. Licence, Charging of ionic liquid surfaces under X-ray irradiation: the measurement of absolute binding energies by XPS, Physical Chemistry Chemical Physics. 13 (2011) 2797–2808. https://doi.org/10.1039/C0CP01587C.

[26] B. Moeini, M.R. Linford, N. Fairley, A. Barlow, P. Cumpson, D. Morgan, V. Fernandez, J. Baltrusaitis, Definition of a new (Doniach-Sunjic-Shirley) peak shape for fitting asymmetric signals applied to reduced graphene oxide/graphene oxide XPS spectra, Surface and Interface Analysis. (2021). https://doi.org/10.1002/sia.7021.

[27] D. Briggs, N. Fairley, XPS of chemically modified low-density polyethylene surfaces: observations on curve-fitting the C 1s spectrum, Surface and Interface Analysis. 33 (2002) 283–290. https://doi.org/10.1002/sia.1212.

[28] A.M. Salvi, J.E. Castle, The intrinsic asymmetry component of the “total background” in XP spectra, J Electron Spectros Relat Phenomena. 94 (1998) 73–87. https://doi.org/10.1016/S0368-2048(98)00083-8.

[29] A.J.S. McIntosh, J. Griffith, J. Gräsvik, Methods of Synthesis and Purification of Ionic Liquids, in: Application, Purification, and Recovery of Ionic Liquids, 2016. https://doi.org/10.1016/B978-0-444-63713-0.00002-X.

[30] E.F. Smith, F.J.M. Rutten, I.J. Villar-Garcia, D. Briggs, P. Licence, Ionic Liquids in Vacuo: Analysis of Liquid Surfaces Using Ultra-High-Vacuum Techniques, Langmuir. 22 (2006) 9386–9392. https://doi.org/10.1021/la061248q.

[31] E.F. Smith, I.J. Villar Garcia, D. Briggs, P. Licence, Ionic liquids in vacuo; solution-phase X-ray photoelectron spectroscopy, Chemical Communications. (2005) 5633. https://doi.org/10.1039/b512311a.

[32] N. Fairley, V. Fernandez, M. Richard-Plouet, C. Guillot-Deudon, J. Walton, E. Smith, D. Flahaut, M. Greiner, M. Biesinger, S. Tougaard, D. Morgan, J. Baltrusaitis, Systematic and collaborative approach to problem solving using X-ray photoelectron spectroscopy, Applied Surface Science Advances. 5 (2021) 100112. https://doi.org/10.1016/j.apsadv.2021.100112.

[33] D.A. Shirley, High-Resolution X-Ray Photoemission Spectrum of the Valence Bands of Gold, Phys Rev B. 5 (1972) 4709–4714. https://doi.org/10.1103/PhysRevB.5.4709.

[34] I. Niedermaier, C. Kolbeck, N. Taccardi, P.S. Schulz, J. Li, T. Drewello, P. Wasserscheid, H.-P. Steinrück, F. Maier, Organic Reactions in Ionic Liquids Studied by in Situ XPS, ChemPhysChem. 13 (2012) 1725–1735. https://doi.org/10.1002/cphc.201100965.

[35] S. Men, D.S. Mitchell, K.R.J. Lovelock, P. Licence, X-ray Photoelectron Spectroscopy of Pyridinium-Based Ionic Liquids: Comparison to Imidazolium- and Pyrrolidinium-Based Analogues, ChemPhysChem. 16 (2015) 2211–2218. https://doi.org/10.1002/cphc.201500227.

[36] V.K. Thorsmølle, G. Rothenberger, D. Topgaard, J.C. Brauer, D.-B. Kuang, S.M. Zakeeruddin, B. Lindman, M. Grätzel, J.-E. Moser, Extraordinarily Efficient Conduction in a Redox-Active Ionic Liquid, ChemPhysChem. 12 (2011) 145–149. https://doi.org/https://doi.org/10.1002/cphc.201000819.

[37] S. Tougaard, Practical algorithm for background subtraction, Surf Sci. 216 (1989) 343–360. https://doi.org/10.1016/0039-6028(89)90380-4.